SAND98-2133C
SAND--98-2133C
CONF-981046--

μA New Approach to Nuclear Microscopy: The Ion-Electron Emission Microscope

RECEIVED
OCT 01 1998
OSTI

B. L. Doyle, G. Vizkelethy*, and D. S. Walsh
Sandia National Laboratories, Albuquerque, NM

B. Senftinger
Staib Instrumente GmbH, Langenbach, FRG

M. Mellon
Quantar Technologies Inc., Santa Cruz, CA

*on leave from Idaho State University

Abstract

A new multidimensional high lateral resolution ion beam analysis technique, Ion-Electron Emission Microscopy or IEEM is described. Using MeV energy ions, IEEM is shown to be capable of Ion Beam Induced Charge Collection (IBICC) measurements in semiconductors. IEEM should also be capable of microscopically and multidimensionally mapping the surface and bulk composition of solids. As such, IIEM has nearly identical capabilities as traditional nuclear microprobe analysis, with the advantage that the ion beam does not have to be focused. The technique is based on determining the position where an individual ion enters the surface of the sample by projection secondary electron emission microscopy. The x-y origination point of a secondary electron, and hence the impact coordinates of the corresponding incident ion, is recorded with a position sensitive detector connected to a standard photoemission electron microscope (PEEM). These signals are then used to establish coincidence with IBICC, atomic, or nuclear reaction induced ion beam analysis signals simultaneously caused by the incident ion.

Barney L. Doyle, Manager
Radiation-Solid Interactions and
Processing Department 1111
MS1056
Sandia National Laboratories
PO Box 5800
Albuquerque, NM, 87185-1056

email: bldoyle@sandia.gov
phone: 505 844 7568
fax : 505 844 7775

DISTRIBUTION OF THIS DOCUMENT IS UNLIMITED

MASTER

1. Introduction

Nuclear microprobe analysis (NMA) is currently performed by focusing MeV ions onto a sample and then scanning the beam in a flying spot analysis. Nuclear, atomic or charge collection signals that are generated by the beam are the detected signal. Analytical NMA has reached a 0.3-0.9 μm limit of beam-spot resolution [1] that can be obtained using a variety of magnetic and electrostatic focusing lenses. No significant improvements in resolution have been reported in over 5 years. The reasons for lack of improvement in NMA resolution are numerous and include 1) difficulty in manufacturing ion optic lenses with required accuracy, 2) difficulties in vibration isolation and 3) the difficulty in focusing high magnetic rigidity and/or poor chromaticity ions from cyclotrons, linacs or older Van de Graaff style electrostatic accelerators.

A different way to perform NMA is proposed here: don't focus the MeV ions at all, but rather, record the position where these ions strike the sample by imaging the secondary electrons that they generate. With this new approach, one uses the MeV ions as a flood beam, and image by projecting the secondary electrons generated by each ion using a Photon Electron Emission Microscope (PEEM). These position signals are recorded with a channeltron+resistive anode Position Sensitive Detector (PSD) and then put into coincidence with the IBA signals caused by the ions as they penetrate the sample. This new technique is called Ion-Electron Emission Microscopy or IEEM.

IEEM ameliorates the corresponding NMA resolution problems listed above in the following fashion: 1) electron lenses are commercially available and PEEMs routinely obtain 40nm resolution, 2) the entire system is small and easier to isolate from vibrations, and 3) since the ions are not focused, any ion can be used for analysis, independent of its mass or energy spread.

In this paper, we describe and characterize the performance of an IEEM prototype device being developed at Sandia National Laboratories. This project was started at Sandia because of the need to perform radiation effects microscopy measurements on a 1.9 MeV/amu heavy ion RFQ linac booster which was recently

DISCLAIMER

This report was prepared as an account of work sponsored by an agency of the United States Government. Neither the United States Government nor any agency thereof, nor any of their employees, makes any warranty, express or implied, or assumes any legal liability or responsibility for the accuracy, completeness, or usefulness of any information, apparatus, product, or process disclosed, or represents that its use would not infringe privately owned rights. Reference herein to any specific commercial product, process, or service by trade name, trademark, manufacturer, or otherwise does not necessarily constitute or imply its endorsement, recommendation, or favoring by the United States Government or any agency thereof. The views and opinions of authors expressed herein do not necessarily state or reflect those of the United States Government or any agency thereof.

DISCLAIMER

Portions of this document may be illegible in electronic image products. Images are produced from the best available original document.

added to our tandem. We start by discussing the physics of secondary electron production by MeV ions, followed by a detailed description of our IEEM system, including the PEEM, PSD and data acquisition system. Some of our initial secondary electron and IBICC maps of simple targets are then shown, and the efficiency/resolution of the system is determined and compared to PEEM operation. We conclude by predicting the ultimate performance characteristics of a perfected IEEM, and forecast its utility in the field of nuclear microscopy.

2. Ion Induced Secondary Electrons

The secondary electron (SE) signal produced by MeV ions has been used for years [2] on traditional (i.e. flying spot) nuclear microprobes, mainly for focussing and identifying a target's region of interest. After all, this is the same physics that underpins scanning electron microscopes (SEMs), and it was only natural that nuclear microscopists would adapt this very common technique. In this mode, the SEs are not imaged, they are just detected using channeltrons or similar detectors. Projection imaging of SEs (similar to what is presented here) and ejected ions has been developed at the Electron Beam Ion Trap (EBIT) facility at Livermore (LLNL) in a new type of time-of-flight SIMS system which uses highly charged low-energy incident ions [3]. Projection imaging of scattered ions has also been proposed by Klein et al. [4]. What we report is the first use of projection secondary electron imaging to record the entry point of individual MeV ions in samples.

The theory of electron and ion-induced SE production is fairly well established, and an excellent review has been written by Schou [5]. The emission of these SEs is thought to involve three stages: 1) ionization by the incident ion and/or energetic secondaries, 2) successful transport of these liberated SEs to the surface, and 3) emission into the vacuum by overcoming a surface potential barrier. In the theory of Sternglass [6], one assumes that if all the electrons ionized (through electronic collisions with the projectile) within the mean-free-path (MFP) of electron scattering from the surface reach the surface, then:

$$\gamma = P\,(\lambda/\cos(\theta))\,(dE/dx)/W \quad , \tag{1}$$

where γ is the SE yield per incident ion, λ is the MFP for electron scattering, θ is the beam's angle of incidence, dE/dx is the electronic stopping power of the incident ion in the target material, W is the ion energy required to ionize an electron, and P is the probability that the electrons reaching the surface can penetrate the potential barrier. The release depth λ is thought to be very shallow (~1-5 nm) for metals but much larger for insulators [7], and have a cosine angular distribution [5]. The energy distribution is peaked at a few eV [8] and the shape, of this distribution is independent of ion and its energy. The peak energy is only slightly higher than that observed of photoelectrons induced by a Hg lamp.

If we separate equation (1) into the parameters of the beam vs. those of the material:

$$\gamma = \Lambda\,(dE/dx)/\cos(\theta) \quad . \tag{2}$$

Hasselkamp ét al. [9] have shown that Λ ranges from 0.07 to 0.13 for smooth silver targets when the stopping power is expressed in units of eV/A. Λ can be reduced significantly due to the presence of surface structures which perturb the uniformity of the local electric field.

3. The Sandia IEEM System

The IEEM system has been installed as a new end station on the original Sandia nuclear microprobe line of Sandia's 6MV Tandem accelerator. Currently, this line is approximately 1.4 m in length from object to aperture slits, 40 cm from aperture slits to the quadrupole doublet, and another 40 cm from the quad to the target. The line utilizes a Dyer Systems QL-300 magnetic quadrupole doublet lens (of the Martin design). As is discussed in the next section, all the work for this paper was performed using the largest aperture setting on the PEEM lens (300 μm) with sample viewing fields up to 250 μm. Clearly, ion strikes that occur outside this field of view may produce IBA signals but no SE position signals. Therefore, in our IEEM

configuration, the purpose of the ion lens is merely to focus the beam sufficiently to limit most ion strikes on the sample to within the field of view of the electron detector. This is especially important for measurements that are sensitive to radiation damage, or other ion fluence effects.

The beams used in this study were 3 MeV H^+ and 24 MeV Si^{+5}, and the targets, which are discussed in detail in the results section, were Si micromachines, Cu TEM grids, and Au-coated PIN Si diodes. The beam's angle of incidence θ was 75° for all experiments. The stopping power of the H and Si ions in the various targets ranged from 2.0 (H on Si) to 982 eV/A (Si on Au) using Ziegler scaling [10]. Referring to eq. (2), and using Λ=0.07 and θ=75°, the SE yield for ion-target combinations was expected to range from ~0.5 to 266 in our experiments.

An IEEM experiment is based on the well-known phenomenon that each ion strike to the sample produces one or more SEs from the near surface region of the target. These electrons are then used to determine the position of the ion strike using the electron lens system of a Photo Electron Emission Microscope or PEEM to accelerate and project these electrons onto a high resolution position sensitive detector (PSD). A schematic diagram of the ion beam – target – PEEM –PSD system is shown in Fig. 1.

3.1 PEEM Electron Projection Lens

The PEEM lens is mounted nearly vertically in the sample chamber, 75° from the ion beam axis. Samples are mounted 75° off normal so that the PEEM detector is always perpendicular to the target, which is a requirement of the objective immersion lens. The entrance to the PEEM is located approximately 4mm from the sample. A high-intensity Hg UV lamp is also mounted in the chamber in position to illuminate the sample and perform standard photon-emission electron microscopy. The target station also includes an ex-vacuo microscopic camera system for viewing the sample.

The field of emission microscopy is approximately 40 years old and has been reviewed by several authors, most recently by Griffith and Engel [11]. Emission microscopy in general is a direct imaging technique. In other words, the image is not formed by scanning or sequential composition; and, therefore, ideally suited for real-time observation. A wide variety of contrast generating mechanisms contribute to distinguish

surface features on a submicron scale. The small energy of the electrons used to form the image accounts for the surface sensitivity of this technique. Ironically, while these contrast mechanisms provide the utility of techniques like PEEM (and electron beam based LEEM), contrast is not desirable for IEEM experiments. This is because IEEM relies on this signal to only provide a measurement of the strike point of an ion. For this reason, the SE yield is the main consideration in an IEEM experiment, and it is actually best if this yield is high and constant across the sample.

The optical column of the basic microscope is formed by several elements shown in Fig. 1: the objective lens, the zoom lens, two projective lenses A and B, and finally the position sensitive detector (PSD). The magnification ranges from 160x to 1600x (when not using projector A which takes this to 8000x) which corresponds to a field of view between 250 and 25 μm. The magnification is set by adjustments to the zoom lens, focusing is performed with the objective lens, and projector B is adjusted so that the field of view fills the PSD.

The specimen surface itself is part of the objective lens. This lens is basically an immersion lens formed by four electrodes (a tetrode lens), the sample surface and a three electrode lens. An accelerating field of the order of several kilovolts per millimeter is applied between the sample and the first element of the lens (transfer voltage). The field strength is a key figure to determine the best lateral resolution. Keeping the sample at ground or at least near ground potential simplifies handling and current measurements; however, it also requires that the whole column is at the transfer potential (up to 15 kV in our case). The homogeneous electric field between the sample and the first lens electrode accelerates the electrons and forms a virtual image below the sample surface. The three electrode lens forms a magnified real image behind the objective lens.

The zoom and two projector lenses account for the final magnification on the image detector. An aperture in the source plane of the projector B limits the field of view. The zoom lens is used to set the total magnification. Two imaging modes are accessible; a low magnification mode and a high magnification mode, and ray traces of these two modes are shown in Fig. 1. High magnification mode means a high field strength in the zoom lens. In this mode, the objective lens forms a real magnified image in front of the

zoom lens, which is further magnified onto the aperture of projector lens B. Low magnification mode means a low field strength in the zoom lens. In this case, there is no real but only a virtual intermediate image formed. Switching between the imaging modes accounts for a flip in the observed image.

The sensitivity of the microchannel plate detector is reduced for higher energy electrons. To improve this sensitivity, a lens that decelerates the electrons to ~1 keV is introduced between the final projector lens and the detector.

Among others, the most prominent factors limiting spatial resolution are lack of mechanical stability, astigmatism and aberrations. To ensure mechanical stability, the PEEM and its chamber sit on a vibration insulation system. Any deviations from cylindrical symmetry along the imaging column can introduce astigmatism. This symmetry is hard to maintain especially in the sample region. To counteract these effects, an octopole stigmator unit is inserted near the back focal plane of the objective lens.

Due to the high field strength at the surface the acceptance angle for the electrons is nearly 90°. This gives rise to a rather large aberration disc or disc of least confusion in the virtual source region. To improve resolution, the total acceptance angle has to be limited by an aperture at the back focal plane of the objective lens (and shown in Fig. 1). Figure 2 shows plots of theoretical resolution (for chromatic aberration only) and transmission efficiency (using ray tracing) versus aperture size for our setup. For these calculations the energy distribution of SEs at the sample was assumed to be peaked at 5 (1) eV, have a 5 (1) eV FWHM for IEEM (PEEM), and be emitted in a cosine pattern. For the results reported below, a 300 μm aperture disc is used, and this should result in a resolution of 0.6 μm with a transmission efficiency of ~30% for IEEM, and 0.2 μm-resolution/100% transmission for PEEM. Use of a 50 μm aperture should improve our IEEM resolution to 0.1 μms with a corresponding loss of transmission to ~1% for IEEM.

3.2 Position-Sensitive Detector (PSD)

Effective secondary electron detection and position recording is critical to the IEEM technique. The system poses several requirements including 1) the efficient detection of electrons, 2) 2-D imaging capability, and

3) time-resolution for the coincidence function and time-of-flight based measurements. A detailed description of this PSD is given in ref. [12].

The detector head consists of a 5-stage, microchannel plate (MCP) electron multiplier directly coupled to a charge-division position encoder (resistive anode encoder, RAE). A schematic of this detector is shown in Fig. 1 with the associated electronics in Fig. 3. The MCP configuration used ensures the high electron gain (approx. 2×10^7) required for high position resolution (100 μm FWHM across 40 mm diameter active area) while maintaining a tight gain pulse-height distribution for single electron initiated events. A PSD resolution of 100 μm at the high PEEM gain of 1600X corresponds to a resolution at the sample of only .06 μm.

In operation, electrons impact the MCP surface located at the final image plane of the PEEM. This results in an electron cascade that is multiplied by the MCP to a measurable level and the resulting charge cloud is electrostatically focused onto the surface of the RAE encoder in an X-Y location corresponding precisely to the location of the incident event on the input MCP. The charge diffusing in the RAE is divided among four collection terminals in a ratio proportional to position in the X and Y axes. The output is fed to a four-channel charge-sensitive amp/shaper module.

From the ratio of the preamp output signals, the readout electronics (the Position Analyzer shown in Fig. 3) computes the X and Y coordinates of each event. These coordinates are output as analog pulses where amplitude is proportional to position. In addition, the position analyzer contains discriminators and pulse-pile-up circuits to veto events that are too low or high in gain, or arrive too close together, to be properly imaged. The XY analog outputs are then connected to the external ADC's used in our multiparameter data acquisition system and to a conventional analog variable persistence X-Y oscilloscope to display real time SE images. The system used has a relatively high instantaneous dynamic counting range extending from the low count rate of the MCP background (10 cps) up to 100,000 detected events/sec (with random arrival statistics, corresponding to 4 usec dead time per event).

The detection efficiency of the MCP's is in the range of 55-80%, where the lower limit is determined primarily by the ratio of microchannel pores to interstitial web area. 100 psec FWHM time resolution for the PSD is obtained by an auxiliary MCP pickoff circuit which senses the time-of-passage of the single event through the MCP.

3.3 Data Acquisition

The detector X and Y outputs are digitized by ADC's and fed to two inputs of an 8 parameter MPA/PC multi-parameter system (see Fig. 3) produced by FAST ComTec [13]. This system operates in list mode, capturing data octets of up to 13 bits of X, 13 bits of Y and the desired number of digital bits from the energy parameters obtained from the separate detectors used for IBA. These data octets are written to fixed disk memory in the PC as sequential data events and can be simultaneously histogrammed in RAM memory and displayed in real time. In addition, the data system offers full time-coincidence capability between parameters, so events are accepted only if they fall into defined time ranges on each parameter. In the results section we show data collected by passing only those signals from the PEEM and an IBICC detector which are in coincidence. For this case, a list of events $\{X,Y,E_{IBICC}\}$ is produced which is exactly the type of list currently used in conventional IBICC measurements.

3.4 Focusing

The initial focus of the PEEM and the region of interest on the sample is found using the Hg lamp. The tilt angle of the target is set to obtain the greatest SE intensity using PEEM. Following these operations, the Hg lamp is extinguished, and the ion beam is steered to and then focused onto the sample within the field of view of the PEEM. The PEEM is then focused again using the secondary electrons produced by ion strikes. The electron focusing (both for PEEM and IEEM modes), ion focusing, and ion beam steering is observed in real time on the XY storage scope. An unintended, but highly desirable feature, of IEEM is its simplicity. The first IEEM image on our system was obtained only a minute after the first beam was introduced into the chamber.

4. Results and Discussion

4.1 SE Images

The very first samples to be examined with the IEEM were 1000-mesh Cu TEM grids (25 μm line spacing) mounted onto our stainless steel target holder. These grids must be considered only very marginal focusing/resolution targets because of their complex shape and the resultant near-surface electric field nonuniformities. Nevertheless, they are convenient, and continue to be used for focusing. Low magnification SE intensity images in both IEEM (a) and PEEM (b) mode are shown in Fig. 4a and b, and intensity line scans are plotted in 4c. The PEEM image was collected with the Hg lamp, and the IEEM image resulted from the exposure of this sample to an unfocussed 24 MeV Si^{5+} beam. One can see from the line scans in 4c that the PEEM-IEEM resolution is quite comparable at 1.1-1.4 μm for these two images. The analysis of high magnification images indicates that our best IEEM resolution to date is 1.0 μm. For PEEM, our best resolution has been 0.8 μm, which is considerably greater than the 0.2 μm expected. Assuming that the PEEM lens and PSD system are working properly, this indicates that we either need a better target to determine resolution or that there are still some parasitic aberration problems (e.g. vibrations or stray EM fields) which need correction. Nevertheless, the 1.0 μm resolution for IEEM is close to the 0.6 μm theoretical calculations shown in Fig. 2.

The contrast of the PEEM image is much greater than that for IEEM. Dust or surface asperities on the grid are quite apparent using PEEM, but not IEEM. This is actually a preferred result, because, as mentioned above, low contrast is desirable for IEEM.

Similar results have been obtained using 3 MeV H^+ beams. In Fig. 5 we plot the sum pulse height distribution obtain from the PSD for PEEM of a Si micromachine target, and IEEM using both H and Si ions on Si targets, and IEEM of the TEM grid using the Si beam. All of these measurements were made with the same saturated MCP bias conditions. The striking differences among these distributions are caused by multiple electrons originating from the same incident ion simultaneously arriving near the same point on the MCP. As the number of such coincident SEs hitting the MCP increases (which happens when going

from the photon and proton beams to the Si beam) the output signal of the MCP also increases as multiple MCP micropores "fire", resulting in an effect similar to pile-up. This effect can be seen in Fig. 5 by the fact that the UV and H induced signals are very similar, while the Si-beam signals both have pronounced higher voltage structures such as peaks or tails. This variation in pulse height distribution from the MCPs can complicate the IEEM measurements because some of the higher voltage pulses are outside of the processing window (shown in Fig. 5) of the Position Analyzer. This has the effect of further reducing the efficiency of the PSD system, but only by 10-20%. On-the-other-hand, this variation could also be used for a new type of contrast microscopy based on SE production rate. It can be seen from Eq. 2 that this contrast would be affected by stopping power, the Λ of the material, and the beam's angle of incidence θ.

4.2 IBICC of PIN diodes

We now move to an example of a true coincidence-based IEEM IBA measurement: Ion Beam Induced Charge Collection (IBICC) of a Au-coated Si PIN photo diode using 24 MeV Si^{5+} and 3 MeV H^{+}. Our initial attempts at this experiment were with uncoated PIN diodes, but there was no measurable SE production from such a target in either the PEEM or IEEM modes. Si diodes have a thin passivation oxide on their surface, and the Hg lamp (~5 eV) cannot excite photoelectrons from SiO_2. Ion induced charging of this layer is suspected as the cause for the low SE signal for IEEM. For diodes with ~0.5 μm of Au deposited onto the surface, the SE signal was extremely intense both in PEEM and IEEM mode.

In Fig. 6, we plot the 24 MeV Si-induced SE+IBICC coincidence intensity image in (a), the mean IBICC signal image in (b) and the sum IBICC signal spectrum in (c). This is an extremely low magnification image, and the size of the Si beam is of the order of 100 μm. This beam is nevertheless well within the field of view of the IEEM using this low magnification setting. A gap appears about a third of the way up on both the intensity and mean IBICC images which was caused by a scratch in the Au layer. The region associated with this scratch apparently did not generate SEs efficiently. The bottom ~1/5th of the mean IBICC image shows a region of greater induced charge. This measurement was taken at the edge of the Au deposit, and this increased IBICC signal corresponds to a thinner Au layer. The effect of this thinner Au

layer is also reflected as the higher peak in the IBICC spectrum (c). The IBICC results with the 3 MeV H beam were much the same, except for a dramatic reduction in the IBICC/SE coincidence rate.

Besides the convenience of these samples, another good reason for performing these IBICC measurements on PIN diodes as that they provide an easy way to measure the net system SE generation and detection efficiency of IEEM. This can be done for a variety of different beams and target materials so long as the beams are entirely contained within the field of view of the IEEM. With this condition observed, every incident ion will produce an IBICC signal, but not all ions will produce detected SEs. This is because 1) they were not produced at the target in the first place, 2) they were lost in transmission through the PEEM lenses, 3) they didn't produce a signal in the MCP, or 4) the MCP signal was outside the processing window of the position analyzer. The system efficiency (SE counts/IBICC counts) for our IEEM is plotted in Fig. 7 for several such measurements using the H and Si beams on the Au-coated diode. Using Eq. 2, we would expect 2 electrons to be made by each 3 MeV proton. Using the 30% transmission through the PEEM and 55% detection efficiency by the PSD, a system efficiency for H on Au should have been 33% which is somewhat higher than the ~10% value measured. For the 24 MeV Si beams on Au, 266 electrons are produced by each ion, and the efficiency should clearly be 100% (i.e., the system should detect at least one SE per incident Si ion). The measurement is ~80%, and is probably low due to reason 4) above and the loss of SE signal near the scratch.

5. Conclusions and Future Activities

The Ion Electron Emission Microscope or IEEM concept was shown to clearly work in a 1-μm resolution mode. This resolution and system efficiency (10s of %) are reasonably close to those predicted by theory. Examples were shown using IEEM for secondary electron emission intensity imaging of simple targets, and it was noted that the MCP signal height could be used for a new type of coincident SE contrast which depends on stopping power and specifics of the target geometry. IBICC measurements were then

performed on PIN diodes. IEEM-based IBICC required coincidence of the charge collection signal with the X-Y signal of the SEs, and this measurement therefore represented a successful proof of principle experiment for the new IEEM technique.

Obviously the success of IEEM as a new type of nuclear microprobe analysis depends on: 1) the number of SEs produced by each impinging ion; 2) the net system efficiency for detecting and recording the position of these electrons; and 3) the detected event probability of the IBA technique used in conjunction with the IEEM. The influence of these three requirements on the future utility of IEEM as a new ion beam microscopy are now addressed:

1) SE production - γ

The SE emission yield γ was found to vary greatly from sample to sample. All grounded metal samples produced copious SE signals, semiconductors such as Si provided adequate signals, but for insulators, virtually no SE signal was observed. In order to perform IBICC on the oxide-passivated PIN diode, it was required to deposit a thin Au layer onto the diode to produce a sufficient number of SEs required for this analysis. The coating did not affect this particular IBICC analysis; however, it is clear that the application of coatings to increase the SE signal will not work in all cases. For example, it is not clear how such a conductive layer would affect the operation and performance of an integrated circuit under IEEM-IBICC analysis. It is also easy to envision analytical uses of IEEM-IBA where the deposit of such a layer would cause elemental interferences with, for example PIXE or RBS signals. On-the-other-hand, there are clearly large classes of materials, such as all metals, where such a coating is not needed, and the IEEM-based IBA analyses should work quite well. Particularly attractive are IBA or charge collection measurements, which require high-energy heavy ions because these will produce several hundred SEs for each ion. This high SE yield will balance reductions in system efficiency expected for ultra high resolution IEEM.

2) System Efficiency - ε

The SE detection efficiency ε, i.e. probability for an electron emitted from the target to be recorded by the PSD, should be 15-20% using the 300 μm aperture. We measured this probability to be less, ~5%, using

protons on Au (see Fig. 7 and remember that the protons produce 2 SEs off Au). The efficiency obtained in our IEEM should increase with operator experience. This increase will enable the use of smaller objective apertures that are required to achieve better resolution. To obtain a 0.1 μm IEEM resolution, Fig. 2 indicates that a 50 μm aperture must be used, and this will decrease the system efficiency to below 1%.

3) IBA Event Probability - φ

After the ion (hopefully) generates a SE that is detected, it should have a relatively high probability φ of doing something in the sample that is detectable. In the case of charge collection measurements, this probability is unity if the region stuck by the ion is a reversed biased pn junction. This is because all ions produce electron-hole (or ion) pairs in semiconductors through the energy loss process, and these signals are all detectable using charge sensitive preamplifiers. This unity detected-event probability is the main reason we first applied IEEM using the IBICC technique. It also provided the best means to measure system efficiency.

Other IBA techniques which have φ=1 include scanning transmission ion microscopy and single event upset imaging of ICs. Unfortunately, most other IBA techniques involve scattering or recoiling collisions that are not usually very probable. These include the usual RBS and Si or He-beam ERD, both which have $\varphi \sim 10^{-6}$ even for major element detection. The event probability for PIXE ranges from 10^{-3} to 10^{-5}. Au beam ERD and He RFS can have φ up to 1%.

The utility of IEEM is limited to those techniques where the product $\gamma\varepsilon\varphi$ is fairly high. Because the PSD can only handle count rates up to 10^5/sec, the count rate of detected IBA events in coincidence with detected SEs, i.e. the IEEM count rate, will be $\gamma\varepsilon\varphi 10^5$. This count rate will remain quite high for the various radiation effects microscopy techniques such as IBICC and SEU Imaging and the transmission energy loss measurements. For Au ERD and He RFS measurements, the count rate is predicted to be in the 100-1000 cps range, but for PIXE the count rate will not exceed 10 cps, which may be too low to utilize.

IEEM still offers numerous advantages to traditional flying-spot nuclear microprobe analysis, and almost all of these advantages stem from the simple fact that keV electrons are a lot easier to focus/project than

MeV ions. IEEM will potentially offer a 10x improvement in image resolution for heavy ion based radiation effects microscopy and IBA. IEEM is particularly attractive for applications on cyclotrons or linacs, which have traditionally been all but excluded from nuclear microanalysis because of poor beam quality.

After improving our system by reducing a sample vibration problem, the IEEM will be moved to a 1.9 MeV RFQ booster which was recently added to the tandem. Here it will be used for research using high energy heavy ions up to 380 MeV Au^{28+}. This research will include 0.1 μm radiation effects microscopy such as IBICC, TRIBICC and SEU-Imaging of advanced radiation hardened ICs designed and manufactured at Sandia. It is also planned to start applying IEEM to microscopically characterize the composition of samples using Au-beam ERD or time-of-flight ERD.

8. Acknowledgements

Sandia is a multiprogram laboratory operated by Sandia Corporation, a Lockheed Martin Company, for the United States Department of Energy under contract DE-AC04-94AL85000.

The authors would like to acknowledge Dan Buller and Steve Renfrow for their assistance in both developing and testing the IEEM system in addition to technical assistance on the accelerator. The U.S. D.O.E under contract DE-AC04-94AL85000 supported this R&D.

8. References

[1] G. Bench, M. Breese, K. Traxel, J Campbell, M. Cholewa, M. Jaksic, E. Swietlicki and B. Doyle, Nucl. Instrum. and Methods B77 (1993) xii.

[2] P.A. Younger and J.A. Cookson, N.I.M. 158 (1970) p193.

[3] A. V. Barnes, E. Magee, A. V. Hamza, T. Schenkel and D. H. Schneider, submitted to Rev. of Sci. Instrum. (1998).

[4] S. Klein, Nucl. Instrum. and Methods B30 (1988) 349.

[5] J. Schou, Scanning Microscopy 2 (1988) 607.

[6] E.J. Sternglass, Phys. Rev. 108 (1957) 1.

[7] J.E. Borovsky and D.M. Suszcynsky, Phys. Rev. A 43 (1991) 1416.

[8] R.G. Musket, J.I Vac. Sci. Technol. 12 (1975) 444.

[9] D. Hasselkamp, K.G. Lang, A. Scharmann, and N. Stiller, Nucl. Instrum. And Methods 180 (1981) 349.

[10] J. Zieler, Appl. Phys. Lett. 31 (1977) 544

[11] O.H. Griffith and W. Engel., *Ultramicroscopy 36, 1 (1991)*

[12] R.W. Odom, B.K. Furman, C.A. Evans, Jr., C.E. Bryson, W.A. Petersen, M.A. Kelly and D.H. Wayne, Analytical Chemistry 55 (1983) 574.

[13] M. Bogovac, I. Bogdanovic, S. Fazinic, M. Jaksic, L. Kukec and W. Wilhelm, Nucl. Instrum. and Meth. B89 (1994) 219.

Figure Captions

Fig. 1. Schematic drawing of the electron optics of a Staib 350 PEEM (Staib Instrumente GmbH, Hagenaustrasse 22, 85416 Langenbach, FRG). Ray traces of both the low and high magnification modes are shown. The system is comprised of a tetroid immersion objective lens, followed by an octapole stigmator lens and three Einsel projection lens (Zoom, A, B). The main aperture is found near the objective lens. A final deceleration lens optimized the energy of the electrons before the strike a position sensitive detector comprised of a stack of 5 microchannelplates (MCP) followed by a resistive anode encoder (RAE).

Fig. 2. . Efficiency and resolution as a function of the PEEM primary aperture diameter for photon induced (PEEM) secondary electrons (SEs), and MeV ion-induced (IEEM) SEs. The efficiency was calculated using an ion ray tracing program, and the resolution resulted from an analytical calculation of chromatic aberration. For the PEEM conditions, the electrons were assumed to have a mean energy of 1eV and a FWHM spread also of 1eV. For the IEEM conditions, these energies were increased to 5eV.

Fig. 3 Schematic of the Sandia IEEM system showing 1) the incident beam of photons or ions striking the sample, 2) the SE projection imaging system consisting of the PEEM and PSD and Quantar 2401B Position Analyzer, and the 8-parameter MPAWIN system (Quantar Technology Inc., 3004 Mission St., Santa Cruz, CA 95060-5700).

Fig. 4 (a) IEEM and (b) PEEM SE intensity images of a 1000 mesh (i.e. 25 μm separation of wires) TEM grid. Line scans are shown in (c). The resolution for both measurements was 1.1-1.2 μm. Considerably less contrast is observed in (a) the IEEM image, which is advantageous to the technique.

Fig. 5 Pulse height spectra of the "Sum" signal from the Position Analyzer for photons, protons and Si ions on various targets (see labels). This signal is just the total electron pulse from the MCP stack. The higher voltage peak and tail for the Si beam is due to coincidence detection of multiple SEs generated by these heavy ions.

Fig. 6 (a) Intensity and (b) mean energy IEEM-IBICC images of a partially focused 24 MeV Si beam hitting a Au-coated PIN Si diode. This is a coincidence measurement between the IBICC signals recorded for individual ion striking the diode and XY position signals generated by the SEs. (c) shows a summed IBICC spectrum. The two peaks in this spectrum suggest different energy losses of the Si in the Au layer before entering the diode.

Fig. 7 The total efficiency of the IEEM system for protons and Si ions on a Au-coated diode. This plot represents a series of measurements similar to that shown in fig. 6. This efficiency is defined as the total number of SEs events divided by the total number of IBICC events. Each measurement was performed with the beam at a different position, but still well within the IEEM field of view. The spread in efficiency is caused by different SE generation rates due to variations in the Au layer.

Figure 1

Object plane

High magnification

Image plane

Low magnification

Objective lens

Zoom lens

Projective lens A

Projective lens B

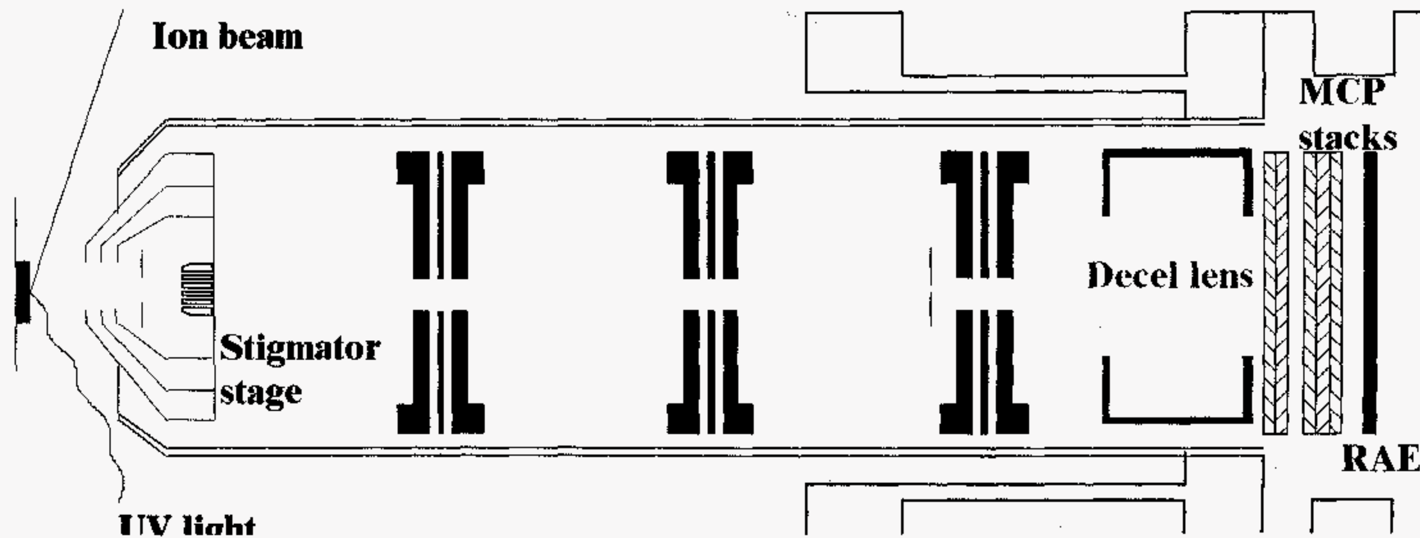

Figure 2

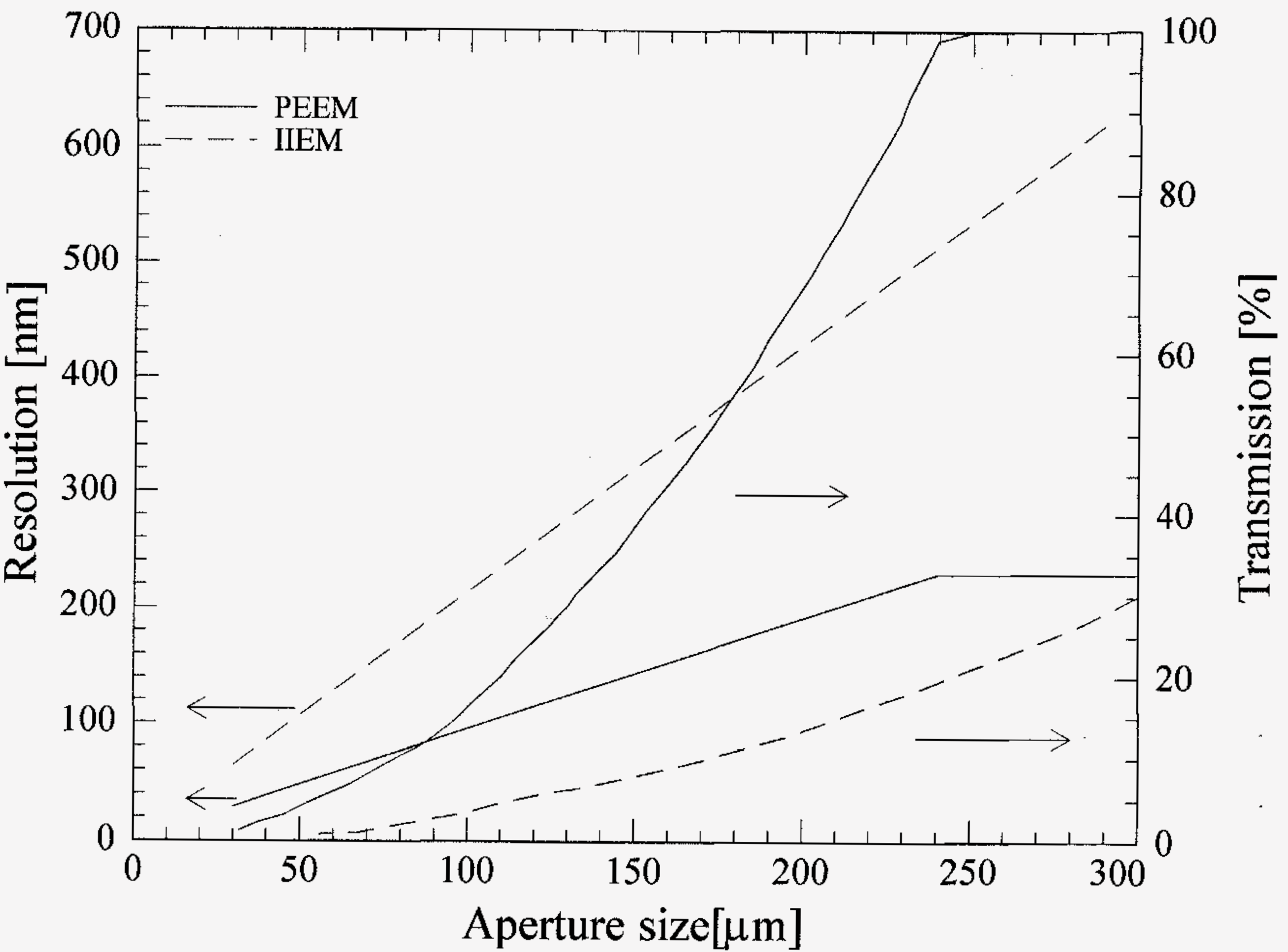

Figure 3

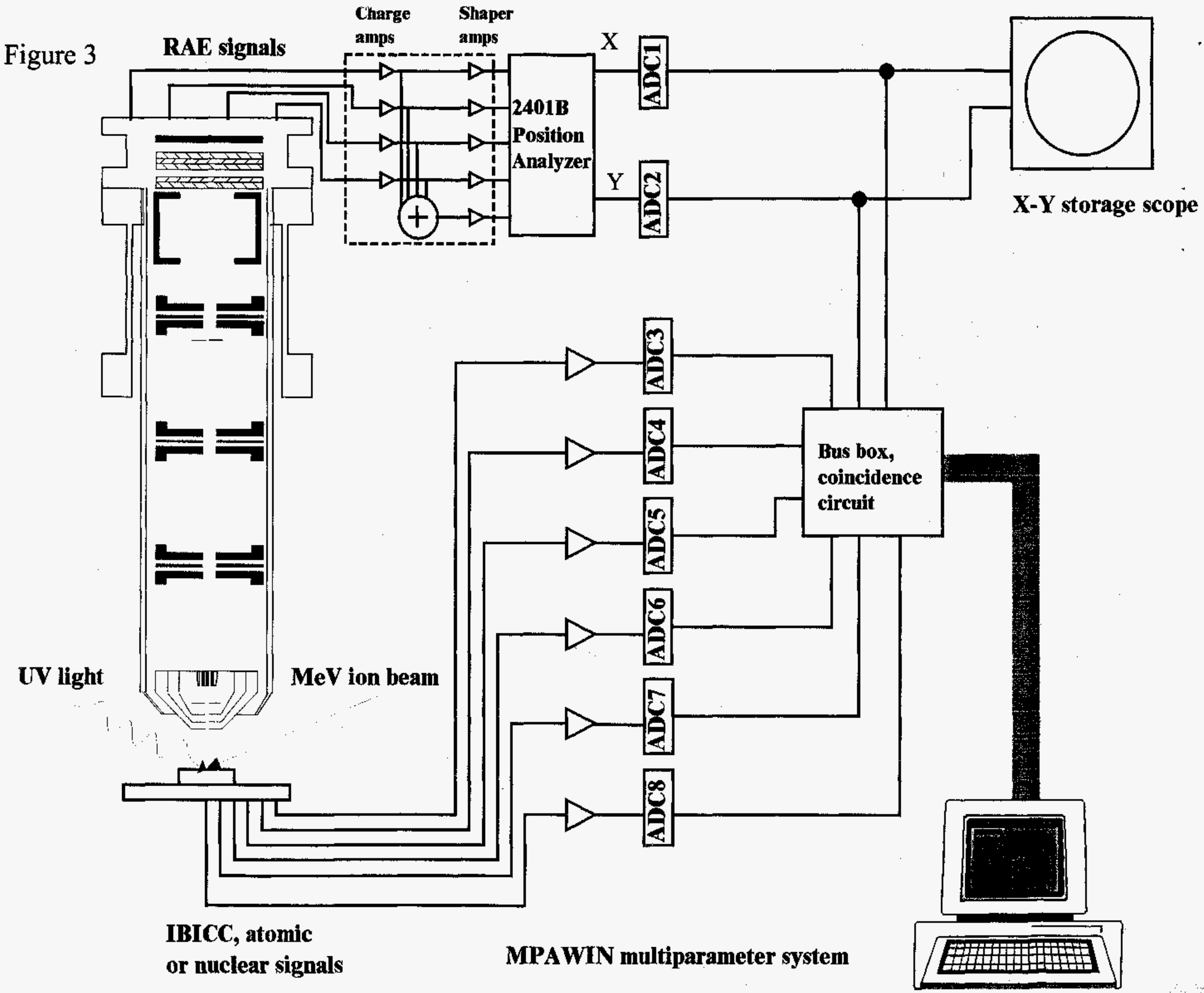

Figure 4

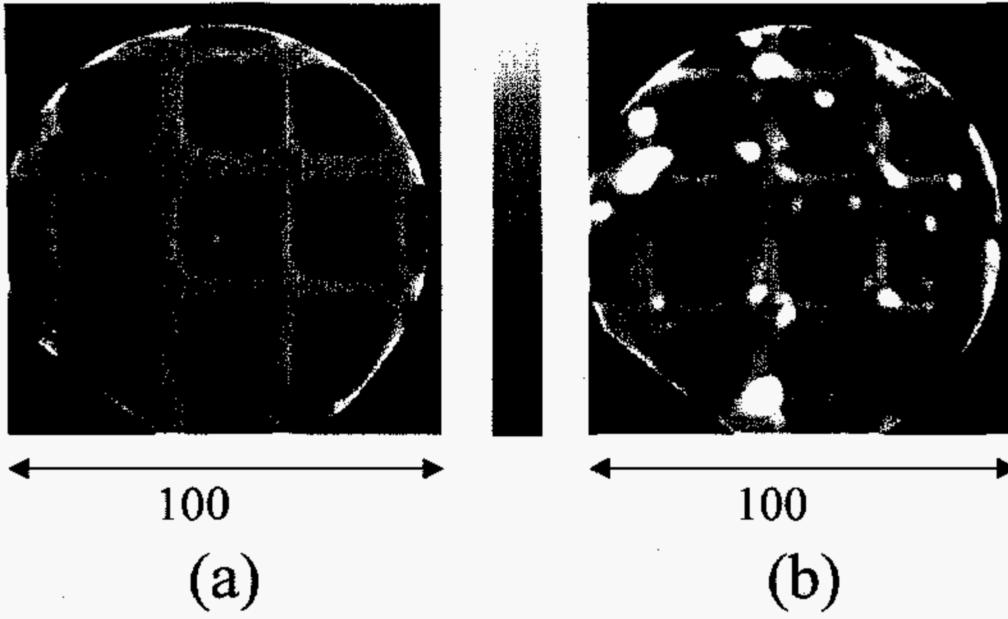

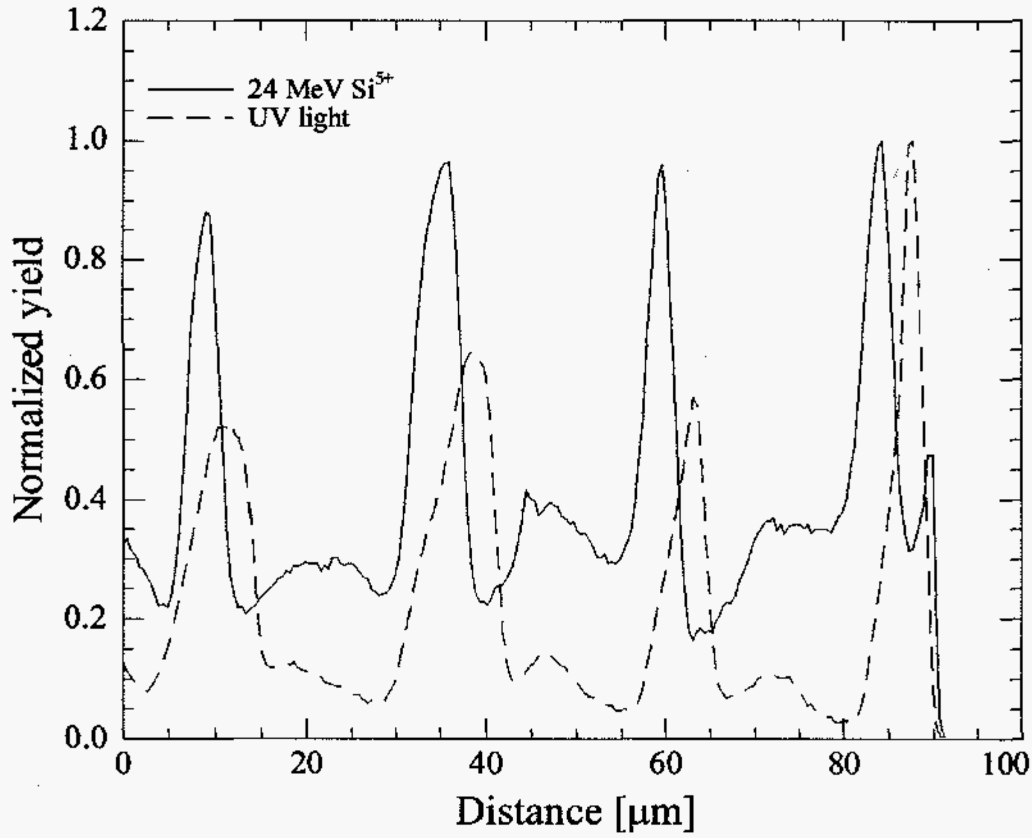

(c)

Figure 5

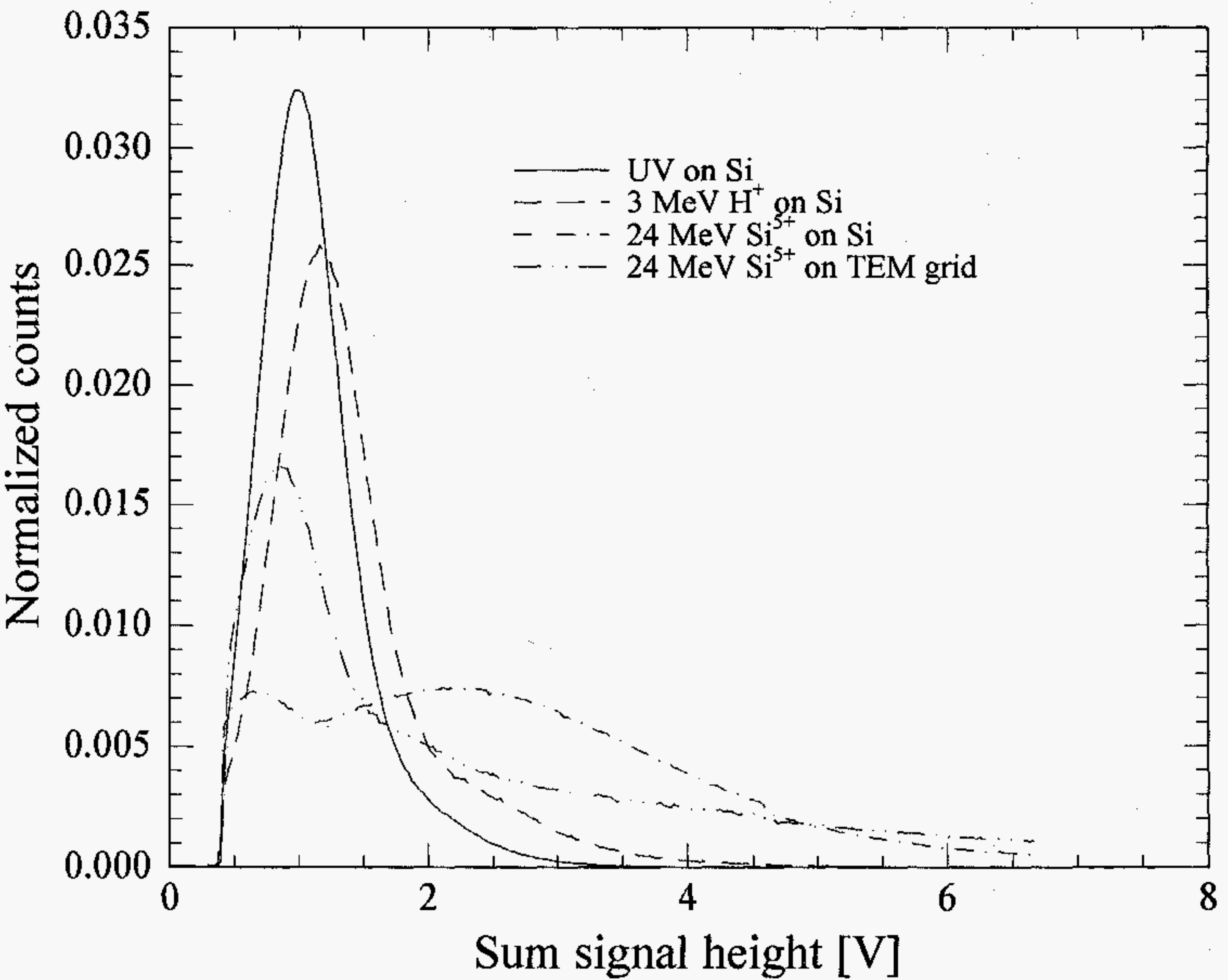

Figure 6

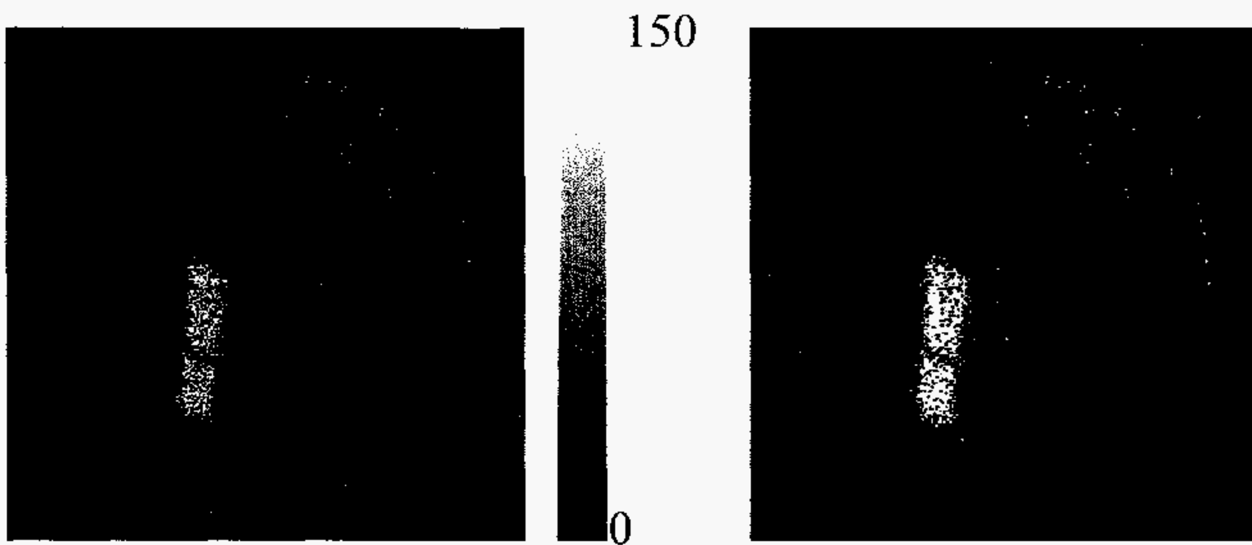

(a) (b)

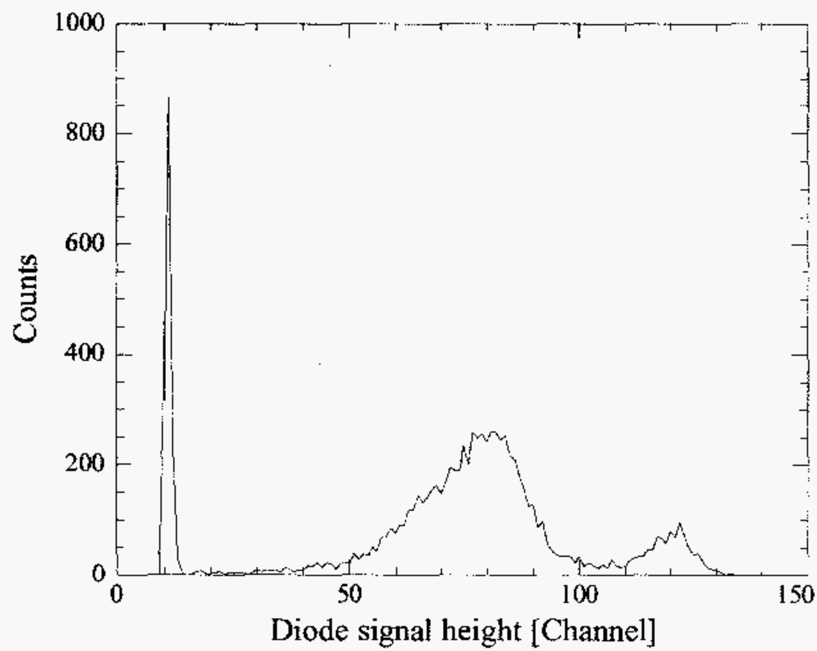

(c)

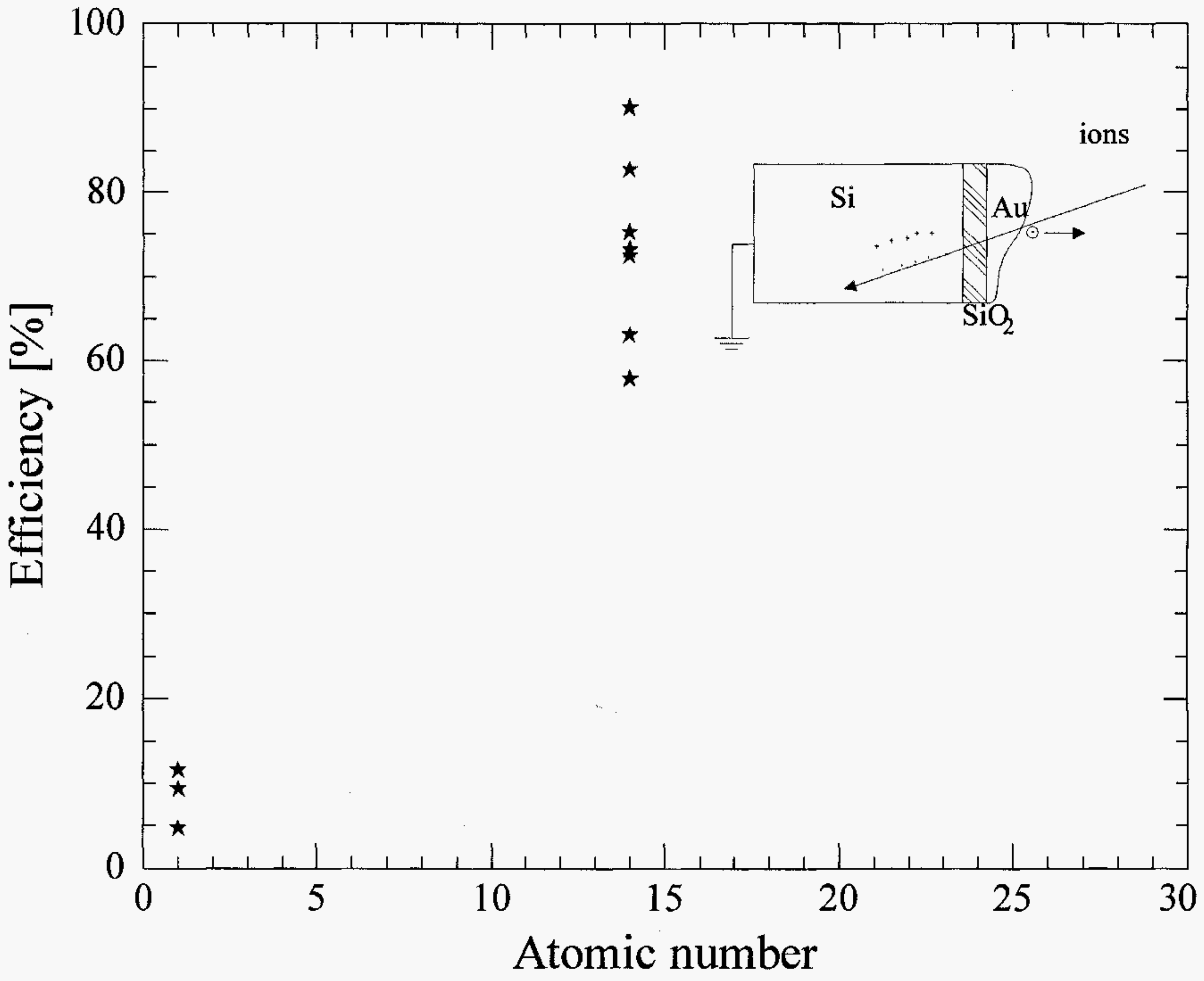
Efficiency [%]
100
80
60
40
20
0
0
5
10
15
20
25
30
Atomic number
ions
Si
Au
SiO_2